



Cite this: *J. Mater. Chem. C*, 2020,  
8, 17025

## Enhanced performance of near-infrared photodetectors based on InGaAs nanowires enabled by a two-step growth method†

Heng Zhang,<sup>a,b</sup> Wei Wang,<sup>a</sup> SenPo Yip,<sup>abc</sup> Dapan Li,<sup>a</sup> Fangzhou Li,<sup>a</sup> Changyong Lan, Fei Wang,<sup>ab</sup> Chuntai Liu<sup>e</sup> and Johnny C. Ho \*<sup>abc</sup>

Because of the tunable bandgap, high carrier mobility and strong interaction with light, ternary III–V nanowires (NWs) have been demonstrated with tremendous potential for advanced electronics and optoelectronics. However, their further performance enhancement and practical implementation are still a challenge in the presence of kinked morphology and surface coating of the nanowires. Here, we report the development of high-performance near-infrared photodetectors based on high-quality InGaAs nanowires enabled by the two-step chemical vapor deposition method. Importantly, the optimized  $\text{In}_{0.51}\text{Ga}_{0.49}\text{As}$  NW devices exhibit excellent photodetector performance at room temperature, with a responsivity of  $7300 \text{ A W}^{-1}$ , a specific detectivity of  $4.2 \times 10^{10} \text{ Jones}$  and an external quantum efficiency of  $5.84 \times 10^6\%$  under 1550 nm irradiation. The rise and decay time constants are as efficient as 480  $\mu\text{s}$  and 810  $\mu\text{s}$ , respectively, constituting a record high performance among all arsenide-based nanowire photodetectors. Large-scale NW parallel-arrayed devices are also fabricated to illustrate their promising potential for next-generation ultrafast high-responsivity near-infrared photodetectors.

Received 10th September 2020,  
Accepted 20th October 2020

DOI: 10.1039/d0tc04330c

rsc.li/materials-c

## Introduction

In the past decade, due to the large surface-to-volume ratio, high carrier mobility, tunable light absorption and considerable subwavelength size effect at room temperature, one-dimensional semiconducting nanowires (NWs) have drawn great attention as intriguing materials for high-performance photodetectors.<sup>1–5</sup> As compared to those of the bulk or thin-film material based counterparts, these NW photodetectors are demonstrated with excellent optoelectronic characteristics with ultrahigh optical gain, controllable spectrum sensitivity, large photoresponse bandwidth and substantial light-to-current conversion efficiency.<sup>5–8</sup> Particularly, ternary III–V semiconductor NWs offer a tunable composition and tailorabile bandgap, making them superior as

active photosensing elements for broadband photodetectors.<sup>9–12</sup> Even though there has been a lot of work focused on exploring NW-based photodetectors in recent years,<sup>13–22</sup> most of the reported NW detectors are restricted in the visible or ultraviolet spectral regions with limited work conducted in the infrared (IR) regime. To date, most of the investigated NW IR photodetectors are dominated by the InAsP and other arsenide-based NW materials.<sup>23,24</sup> For example, indium gallium arsenide ( $\text{In}_x\text{Ga}_{1-x}\text{As}$ ) NWs have always been utilized in the community owing to their variable band gap, ranging from the near-IR to the IR region (0.34–1.42 eV).<sup>25–27</sup> In addition, the properties of high electron mobility and small leakage current also enable these  $\text{In}_x\text{Ga}_{1-x}\text{As}$  NWs being widely used for other optoelectronic devices in near-IR emission lasers, photovoltaics, and field-effect transistors.<sup>28,29</sup> However, the device performance of InGaAs NW IR photodetectors is still far from satisfactory for practical utilization, leaving much room for improvement and comprehensive investigation.<sup>30</sup> Based on our previous work, we have successfully fabricated highly-crystalline, high-mobility and highly-dense  $\text{In}_x\text{Ga}_{1-x}\text{As}$  NWs using a novel two-step chemical vapor deposition (CVD) method.<sup>31,32</sup> In this work, we further utilize these high-quality  $\text{In}_x\text{Ga}_{1-x}\text{As}$  NWs for high-performance photodetectors in the IR optical communication region (1550 nm). As compared with the typical single-step growth, the  $\text{In}_x\text{Ga}_{1-x}\text{As}$  NWs enabled by the two-step CVD growth are observed with the reduced kinked morphology and minimized surface coating issue, while

<sup>a</sup> Department of Materials Science and Engineering, City University of Hong Kong, Kowloon 999077, Hong Kong SAR, China. E-mail: johnnyho@cityu.edu.hk

<sup>b</sup> State Key Laboratory of Terahertz and Millimeter Waves,

City University of Hong Kong, Kowloon 999077, Hong Kong SAR, China

<sup>c</sup> Shenzhen Research Institute, City University of Hong Kong, Shenzhen 518057, China

<sup>d</sup> State Key Laboratory of Electronic Thin Films and Integrated Devices, and School of Optoelectronic Science and Engineering, University of Electronic Science and Technology of China, Chengdu 610054, China

<sup>e</sup> Key Laboratory of Advanced Materials Processing & Mold (Zhengzhou University), Ministry of Education, Zhengzhou 450002, China

† Electronic supplementary information (ESI) available. See DOI: 10.1039/d0tc04330c

maintaining the good crystallinity and uniform distribution of constituents within the NW body. For the optimized  $\text{In}_{0.51}\text{Ga}_{0.49}\text{As}$  NWs, when they are configured into individual NW devices, they deliver an excellent photodetector performance at room temperature, with a responsivity of  $7300 \text{ A W}^{-1}$ , a specific detectivity of  $4.2 \times 10^{10}$  Jones, an external quantum efficiency (EQE) of  $5.84 \times 10^6\%$  and a response time of  $480 \mu\text{s}$  under IR illumination (1550 nm) at a bias voltage of 0.5 V. This efficient response in the hundreds of microsecond range is rather competitive among all NW IR photodetectors reported in the literature. Moreover, these NWs can as well be fabricated into NW parallel array-based devices, demonstrating their technological potential as candidate materials for next-generation, ultrafast and efficient room-temperature photodetectors.

## Results and discussion

Here, the  $\text{In}_x\text{Ga}_{1-x}\text{As}$  NWs were synthesized using a catalytic solid-source CVD method reported by our group previously.<sup>31,32</sup> Both single-step and two-step growth methods were utilized to compare and explore optoelectronic properties for these two kinds of  $\text{In}_x\text{Ga}_{1-x}\text{As}$  NWs obtained, respectively. In brief, the two-step approach has an additional nucleation step at a higher temperature before the regular growth step during the conventional single-step CVD growth. As shown in the scanning electron microscopy (SEM) image in Fig. 1a, this two-step method can significantly reduce the kinked morphology, defect density, as well as surface coating around NWs as compared with the ones obtained by the single-step method (ESI† Fig. S1). The two-step grown  $\text{In}_x\text{Ga}_{1-x}\text{As}$  NWs are typically found to have a length exceeding 10  $\mu\text{m}$  and an average diameter of 30 nm

uniformly along the length of the NWs. In order to further characterize the NWs grown by this two-step technique, high-resolution TEM (HRTEM) was utilized to study the structural properties of these NWs. As depicted in Fig. 1b and c, a spherical catalytic seed is observed at the tip of a typical NW, which confirms the VLS growth mechanism. The corresponding FFT pattern further illustrates its single crystalline zinc blende (ZB) structure and its preferential growth orientation in the  $\langle 311 \rangle$  direction with no significant amount of stacking faults or twin-plane polytypic defects in the samples.

The spacings between the adjacent lattice planes are found to be 0.29 and 0.18 nm for  $\{200\}$  and  $\{311\}$  planes, respectively, which are in good agreement with the results found before in the previous study.<sup>32</sup> Also, NW stoichiometry can be assessed using the energy-dispersive X-ray spectroscopic (EDS) spectrum as given in Fig. 1d. All of these indicate the good crystallinity of NWs grown using this two-step technique. Moreover, to assess the NW composition-dependent properties,  $\text{In}_x\text{Ga}_{1-x}\text{As}$  NWs with different chemical stoichiometries of In and Ga have also been synthesized by mixing InAs and GaAs powders in various ratios as the precursor source. The chemical composition of the obtained NWs could then be evaluated by using EDS measurement, where they are found to be  $\text{In}_{0.22}\text{Ga}_{0.78}\text{As}$ ,  $\text{In}_{0.34}\text{Ga}_{0.66}\text{As}$ , and  $\text{In}_{0.43}\text{Ga}_{0.57}\text{As}$  (Fig. S2, ESI†). By carefully adjusting the growth parameters, such as nucleation temperature, growth temperature, and growth time, the as-grown NWs can have the desirable morphology in all composition ranges. To shed light onto the photodetection properties of the as-grown nanowires, field-effect transistor (FET) based photodetectors were fabricated by using Ni ( $\sim 50 \text{ nm}$ ) source/drain (S/D) metal contacts in a common back-gated configuration (50 nm thermal oxide as the gate dielectric and heavily B-doped

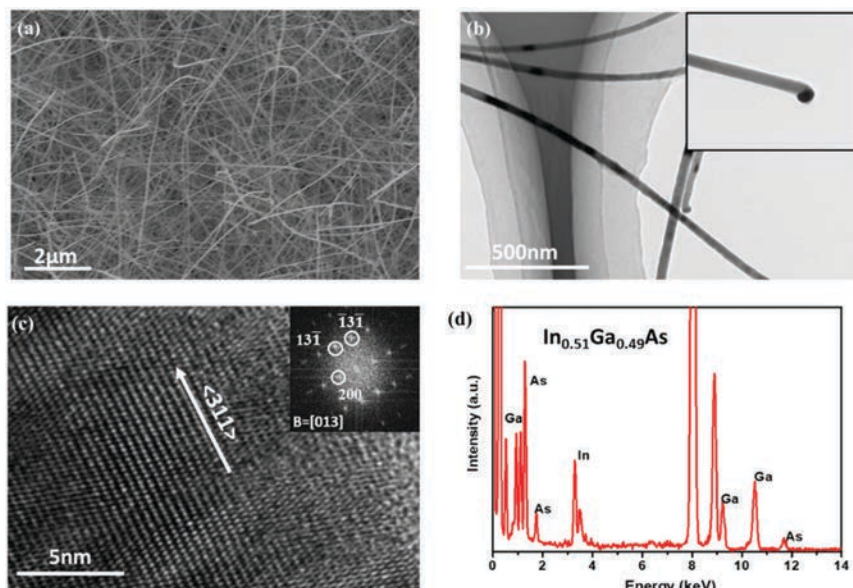


**Fig. 1** Morphology, crystal structure and elemental analysis of the two-step grown  $\text{In}_{0.51}\text{Ga}_{0.49}\text{As}$  NWs. (a) Scanning electron microscopy image; (b and c) transmission electron microscopy image (inset of b shows the tip image; inset of c gives the Fast Fourier Transform pattern of the NW body, showing a zinc blende structure with the  $\langle 311 \rangle$  growth direction); and (d) energy dispersive X-ray spectroscopy spectrum.

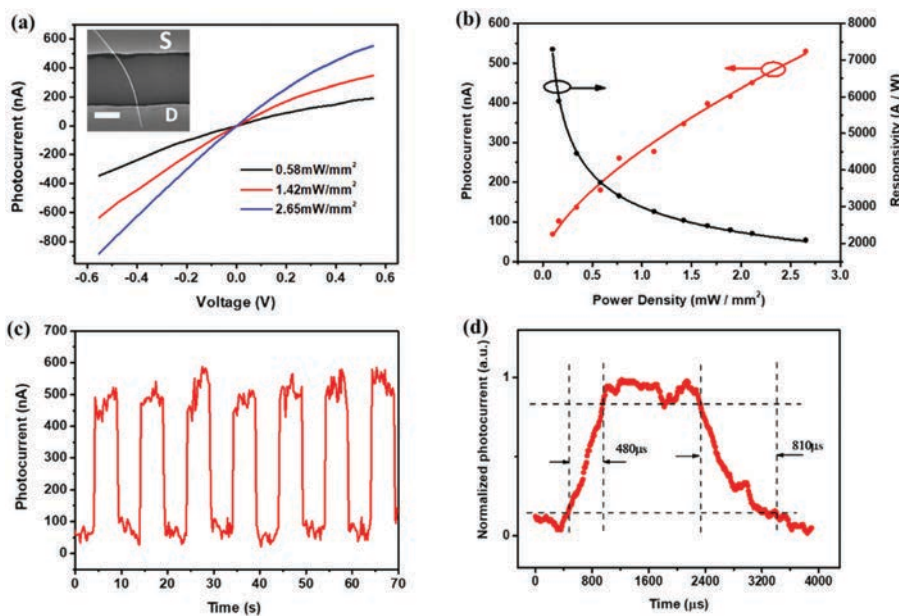


**Fig. 2** Photodetection properties of a typical  $\text{In}_{0.51}\text{Ga}_{0.49}\text{As}$  NW (1550 nm laser) grown using the two-step method. (a) Current–voltage curves under the illumination intensity of 0.58, 1.42 and 2.65  $\text{mW mm}^{-2}$ , respectively. The inset shows the SEM image of the photodetector with the scale bar of 1  $\mu\text{m}$ ; (b) photocurrent and responsivity as a function of the incident illumination intensity. (c) Photoresponse of the NW photodetector under the illumination intensity of 2.65  $\text{mW mm}^{-2}$ . The chopped frequency is 0.1 Hz. (d) A high-resolution transient photoresponse of the device to illustrate the rise time and decay time constants. In the panel b to d, the source-drain bias is 0.5 V. The gate bias is  $-1\text{ V}$  for all measurements.

Si substrate as the gate) as shown in the illustrative device schematic in the Fig. 2a inset. The electrical performance of a representative FET, consisting of an individual two-step grown  $\text{In}_{0.51}\text{Ga}_{0.49}\text{As}$  NW as the channel material with the diameter of  $d \sim 24\text{ nm}$  (NW diameter  $\sim 26\text{ nm}$  with a  $\sim 2\text{ nm}$  native oxide shell) and a channel length of  $L \sim 2.64\text{ }\mu\text{m}$ , is shown in the ESI† Fig. S3. The obtained n-type semiconducting behaviors (*i.e.* output and transfer characteristics) of the NW devices were consistent with previous work.<sup>31,32</sup> Furthermore, the cost-effective and efficient IR photodetection at room temperature is still a technological challenge due to the lack of appropriate active photosensing materials. Impressively, the fabricated  $\text{In}_x\text{Ga}_{1-x}\text{As}$  NW photodetectors here have been proved with the efficient photoconductive characteristics towards the short-wave IR regime (*i.e.* optical communication region at 1550 nm). Fig. 2a displays the corresponding current–voltage ( $I$ – $V$ ) characteristics measured under various power intensities (*i.e.* 0.58, 1.42, 2.65  $\text{mW mm}^{-2}$ ) of 1550 nm light irradiation, respectively, under a gate bias,  $V_{\text{gs}}$ , of  $-1\text{ V}$ . The linear  $I$ – $V$  relationship demonstrates the ohmic-like contact behavior of the photodetector device, which favors the photogenerated carrier collection even facing a risk of the oxidation of Ni at the interface when using Ni as the electrodes. In this way, the Ni oxidation effect could be neglected here, where Ni metals are widely employed in many other NW devices.<sup>21,22,31–33</sup> Based on the  $I$ – $V$  characteristics, the excellent photoresponse behavior of the device can be observed with various incident intensities as the output current increases accordingly when the illumination intensity increases. To further figure out the device characteristics of these NW detectors, the relationship between the photocurrent,  $I_{\text{ph}}$ , (defined as the current difference between

the illuminated state and the dark state) and the intensity of light is assessed and compiled in Fig. 2b. The dependence can be fitted by the following sublinear relationship:

$$I_{\text{ph}} = A\Phi^{\alpha} \quad (1)$$

where  $A$  and  $\alpha$  are the fitting parameters and  $\Phi$  is the light intensity. After the fitting process, the value of  $\alpha$  is estimated to be 0.65, revealing the sublinear relationship between photocurrent and light intensity, which is often observed in metal-oxide-based photoconductors because of the complex processes of electron–hole generation, trapping and recombination in the semiconductors.<sup>34,35</sup> On the other hand, the photoresponsivity,  $R$ , is another important parameter to assess the photodetector performance, which can be expressed as:

$$R = \frac{I_{\text{ph}}}{\Phi S} \quad (2)$$

where  $S$  is the active area of the photodetector. According to eqn (1) and (2),  $R$  should be proportional to  $\Phi^{\alpha-1}$ , which is shown in Fig. 2b. In this case, at a low incident intensity of 0.1  $\text{mW mm}^{-2}$  and a source-drain bias,  $V_{\text{ds}}$ , of 0.5 V, the value of  $R$  is calculated to be  $7300\text{ A W}^{-1}$ . Based on these dependences, several other key performance parameters, such as external quantum efficiency (EQE) and specific detectivity ( $D^*$ ) of the NW device can also be assessed. In general, these parameters can be defined as:

$$\text{EQE} = R \frac{hc}{e\lambda} \quad (3)$$

$$D^* = R \sqrt{S/2eI_{\text{dark}}} \quad (4)$$

**Table 1** Comparison of performance metrics of single As-based nanowire IR photodetectors reported in the literature

Materials	Incident wavelength (nm)	Responsivity (AW <sup>-1</sup> )	Operating temperature	Dark current/bias voltage	EQE (%)	Response speed	Ref.
GaAs	400–1200	—	RT	—	—	—	36
InAs	632–1470	5.3 × 10 <sup>3</sup>	RT	~1 nA/2 V	—	—	20
InAsP	700–3500	5417	RT	0.2 μA/0.5 V	3.95 × 10 <sup>5</sup>	—	23
InGaAs	1100–2000	6.5 × 10 <sup>3</sup>	RT	144 nA/0.5 V	5.04 × 10 <sup>5</sup>	280 ms	30
GaAsSb	1100–1660	2.37	77 K–RT	<100 nA/0.1 V	—	—	24
GaAsSb	1150–1550	1.7 × 10 <sup>3</sup>	RT	—	1.62 × 10 <sup>5</sup>	60 ms	37
GaSb/GaInSb	780–2250	1 × 10 <sup>3</sup>	RT	—	8.5 × 10 <sup>4</sup>	2 ms	15
InGaAs	1550	5.75	77 K	—	—	—	38
InGaAs	1550	7.3 × 10 <sup>3</sup>	RT	900 nA/0.5 V	5.84 × 10 <sup>6</sup>	480 μs	This work

where  $h$  is Planck's constant,  $\lambda$  is the illumination wavelength,  $e$  is the electronic charge,  $c$  is the velocity of light and  $I_{\text{dark}}$  is the dark current. Accordingly, the values of EQE and  $D^*$  can be determined to be  $5.84 \times 10^6\%$  and  $4.2 \times 10^{10}$  Jones. Such results show the excellent sensitivity of our devices for IR photodetection. These measured performance parameters are already comparable to those of the state-of-the-art arsenide-based III–V NW photodetectors as listed in Table 1.

At the same time, it is also important to evaluate the capability of  $\text{In}_x\text{Ga}_{1-x}\text{As}$  NW photodetectors to follow a fast varying optical signal; therefore, time-resolved photocurrent measurements were conducted by periodically modulating the illumination cycle of the near-IR laser of 1550 nm. Explicitly, Fig. 2c depicts the photocurrent trace of the device under a light intensity of  $2.65 \text{ mW mm}^{-2}$  with a chopping frequency of 0.1 Hz at  $V_{\text{ds}} = 0.5 \text{ V}$  and  $V_{\text{gs}} = -1 \text{ V}$ . It is obvious that the efficient on–off switching behavior indicates the outstanding reproducibility and stability of the NW device. The device on- and off-state currents for each cycle shown here vary within  $450 \pm 90$  and  $30 \pm 20 \text{ nA}$ , respectively, within the noise level, which suggests the stable optical reversibility over the measured time interval. The possible origins of the observed fluctuations could be caused by the absorption/desorption of surface molecules. The photocurrent values reveal that no pumping or priming effects need to be considered for the explored time scale. Furthermore, a digital oscilloscope was connected to the measurement system in order to monitor and capture the fast-varying photocurrent signals,<sup>39,40</sup> which helped to accurately evaluate the rise and decay time constants of the device. Fig. 2d shows the high-resolution time-dependent photocurrent response of the device at a chopping frequency of 300 Hz. Evidently, a rise time of  $480 \mu\text{s}$  and a decay time of  $810 \mu\text{s}$  were obtained. Typically, we consider the time it takes for the net photocurrent to increase from 10% to 90% (or decrease from 90% to 10%) as the rise time (or decay time). This efficient response in the hundreds of microsecond range represents one of the fastest responses among all of the arsenide-based NW IR photodetectors reported in the literature (Table 1). The relatively fast response speed indicates the fast generation and recombination process of electron–hole pairs that occurred in the NWs when under illumination, which could be attributed to the excellent NW crystal quality and fewer surface states in contrast to those nanowires grown by the single-step method. As compared to the conventional

single-step CVD that contains only one regular growth step, the two-step approach has an additional nucleation step at a higher temperature before the regular growth step. Regarding the  $\text{In}_x\text{Ga}_{1-x}\text{As}$  NW system, this two-step method can significantly reduce the kinked morphology, defect density, and surface coating around NWs in contrast to the ones obtained by the single-step method (ESI† Fig. S1). As shown in the ESI† Fig. S4a, the time-resolved photocurrent measurement was also performed for the device with the  $\text{In}_{0.51}\text{Ga}_{0.49}\text{As}$  NW channel grown by the single-step method under a light intensity of  $2.65 \text{ mW mm}^{-2}$  and a chopping frequency of 0.04 Hz. The photocurrent is observed to have a larger fluctuation and lower value than those of the device with the two-step grown NW. Notably, the photoresponse speeds are found to have the rise and decay time constants of 160 ms and 230 ms, respectively (ESI† Fig. S4b), being much slower as compared to the ones of the two-step grown NW. As a result, it is witnessed that the two-step grown  $\text{In}_x\text{Ga}_{1-x}\text{As}$  NWs possess much better optoelectronic properties than those of single-step grown NWs due to the superior NW crystal quality and fewer surface states.

As one of the ternary alloy NWs, the  $\text{In}_x\text{Ga}_{1-x}\text{As}$  NWs have been proven to yield a uniform stoichiometric system that can be synthesized using the facile growth method here.<sup>31,32</sup> Hence, the bandgap of the NWs can be manipulated by simply adjusting their chemical stoichiometry. In this case, it is important to investigate the relationship between the composition of  $\text{In}_x\text{Ga}_{1-x}\text{As}$  NW channels and the IR photodetector performance. As presented in Fig. 3, Table 2 and Fig. S5 (ESI†), it is clear that the IR photoresponse of the NW devices would enhance substantially when the In concentration of the NW channel increases accordingly. This enhancement is mostly attributed to the reduced bandgap as well as the improved absorption coefficient under 1550 nm irradiation, where the corresponding bandgap changes have been clearly illustrated in the previous work.<sup>32</sup> Also, according to the definition of current density for an n-type semiconductor,

$$I_{\text{ph}} = nq\mu ES \quad (5)$$

where  $n$  is the electron density,  $\mu$  is the electron mobility,  $E$  is the applied electric field and  $S$  is the cross-sectional area of a NW.<sup>41,42</sup> This way, as the In concentration of the NW increases, the electron mobility would show the nearly monatomic increase from Ga-rich devices (averaging  $\sim 320 \text{ cm}^2 \text{ V}^{-1} \text{ s}^{-1}$ ) to In-rich devices (averaging  $\sim 2700 \text{ cm}^2 \text{ V}^{-1} \text{ s}^{-1}$ );<sup>32</sup> therefore,

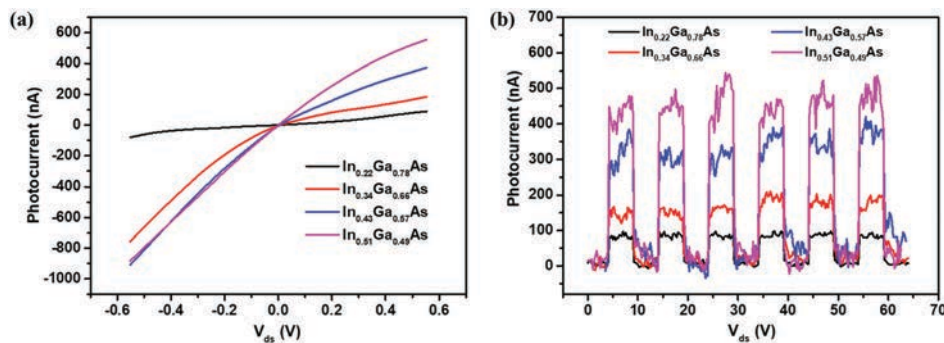


**Fig. 3** Photodetection properties of the single  $\text{In}_x\text{Ga}_{1-x}\text{As}$  NW grown by the two-step method with different NW compositions (1550 nm laser). (a) Current–voltage curves of  $\text{In}_x\text{Ga}_{1-x}\text{As}$  nanowire devices. (b) Transient response of the single  $\text{In}_x\text{Ga}_{1-x}\text{As}$  NW photodetector devices. The illumination intensity is  $2.65 \text{ mW mm}^{-2}$  for all the measurements.

**Table 2** The photodetection performance of  $\text{In}_x\text{Ga}_{1-x}\text{As}$  nanowire devices (1550 nm,  $2.65 \text{ mW mm}^{-2}$ ). EQE stands for external quantum efficiency

InGaAs photodetector (1550 nm)	Responsivity ( $\text{AW}^{-1}$ )	EQE (%)	Detectivity (Jones)	Rise time ( $\mu\text{s}$ )	Decay time ( $\mu\text{s}$ )
$\text{In}_{0.51}\text{Ga}_{0.49}\text{As}$	2084	$1.67 \times 10^6$	$1.2 \times 10^{10}$	480	810
$\text{In}_{0.43}\text{Ga}_{0.57}\text{As}$	1248	$9.93 \times 10^5$	$7.2 \times 10^9$	490	780
$\text{In}_{0.34}\text{Ga}_{0.66}\text{As}$	748	$5.95 \times 10^5$	$4.31 \times 10^9$	510	850
$\text{In}_{0.22}\text{Ga}_{0.78}\text{As}$	372	$2.91 \times 10^5$	$2.05 \times 10^9$	530	870

the photocurrent is anticipated to increase for the increasing In concentration (Fig. 3). At the same time, the bandgap energy of the  $\text{In}_{0.51}\text{Ga}_{0.49}\text{As}$  NW can be estimated from the absorption spectrum by linear extrapolation of the absorption edge to zero absorbance (ESI† Fig. S6). This absorption onset value is observed to be very close to 1550 nm, further indicating the appropriate bandgap energy value of  $\text{In}_{0.51}\text{Ga}_{0.49}\text{As}$  NWs for the optimal photodetection under 1550 nm irradiation. As a result, the  $\text{In}_{0.51}\text{Ga}_{0.49}\text{As}$  NWs are confirmed to be the ideal device channel material as they give the best photoresponse properties among all the different NW compositions.

In order to further demonstrate the feasibility of utilizing these NW photodetectors for the large-scale device integration, the well-established NW contact printing method<sup>33,43,44</sup> has been employed to fabricate InGaAs NW parallel array devices in order to evaluate their photoresponse characteristics in the 1550 nm regime (Fig. 4a inset and ESI† Fig. S7). The  $\text{In}_{0.51}\text{Ga}_{0.49}\text{As}$  NWs grown *via* the two-step method are chosen as the effective materials for the utilization of parallel arrayed devices due to their enhanced photodetection properties discussed above. Typical *I*-*V* characteristics of the fabricated photodetector under different light intensities (*i.e.* 0.08, 1.05

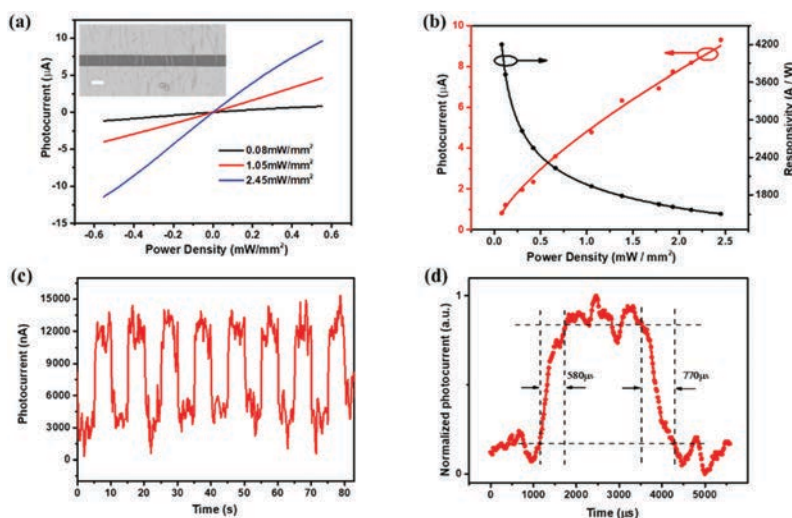


**Fig. 4**  $\text{In}_{0.51}\text{Ga}_{0.49}\text{As}$  NW parallel array devices. (a) Current–voltage curves under the different illumination intensities of  $0.08$ ,  $1.05$  and  $2.45 \text{ mW mm}^{-2}$ , respectively. The inset shows the corresponding scanning electron microscopy image of the device. The scale bar is  $2 \mu\text{m}$ ; (b) photocurrent and photoresponsivity of the device as a function of the light intensity; (c) transient curve of the device with the modulated illumination (1550 nm,  $2.45 \text{ mW mm}^{-2}$ ); (d) high-resolution transient curve of the device with the modulated illumination (1550 nm,  $2.45 \text{ mW mm}^{-2}$ ).

and  $2.45 \text{ mW mm}^{-2}$ ) are illustrated in Fig. 4a. It is obvious that there is a linear relationship of the  $I$ - $V$  curves exhibited from the device, suggesting the ohmic contact property for the efficient photogenerated carrier collection. On the other hand, the output current increases with increasing intensity accordingly. As depicted in Fig. 4b, the values of  $R$  and  $D^*$  are found to be about  $4200 \text{ A W}^{-1}$  and  $1.6 \times 10^9 \text{ Jones}$ , respectively, at a low incident light intensity of  $0.08 \text{ mW mm}^{-2}$  with the  $V_{ds}$  of  $0.5 \text{ V}$ . As compared with the single NW photodetector, these  $R$  and  $D^*$  values indicate a slight reduction in the photodetector performance probably because of the improper alignment of the NW arrays, NW-to-NW variation and breakage of NWs within the device channel. In any case, the time-resolved photoresponse of the NW parallel array device still gives the reproducible switching on-off behavior. More importantly, the ultrafast rise and decay time constants with the value of  $580$  and  $710 \mu\text{s}$ , respectively, are observed for these NW parallel array devices. All these findings suggest that once the NW parallel array density and alignment are further optimized, together with the channel length scaling, the device performance of InGaAs NW parallel array photodetectors can be substantially improved in the future.

Simultaneously, the photogain,  $G$ , of a photoconductor can be estimated as the number of charge carriers passing between the electrodes for each photon absorbed per second, where the phenomenon can be described with the following relationship:

$$G = \tau/t_r \quad (6)$$

where  $\tau$  is the lifetime of photo-generated free carriers and  $t_r$  is the transit time of carriers between two electrodes. Since there is always a high density of surface states that existed on the NW surface due to the large surface-to-volume ratio and unpassivated surface, the Fermi energy level of the NW can be pinned at the surface forming a depletion layer. This layer would result in the more effective separation of photogenerated electrons and holes, and yield the longer lifetime of free carriers.<sup>45</sup> On the other hand, the transit time of InGaAs NWs is found to be short owing to their high electron mobility. For both reasons, the photoconductors made from InGaAs NWs can obtain a high gain value here. As responsivity can also be expressed with the relationship of  $G$  in the following:

$$R = e (\eta \lambda / hc) G \quad (7)$$

where  $\eta$  is the quantum efficiency and the lifetime of photo-generated free carriers,  $\tau$ , can be estimated from eqn (6) and (7). This way, it can be rewritten as  $\tau = R (hc/\eta\lambda) (1/e) t_r$ . Specifically, considering a bias of  $0.5 \text{ V}$ , a channel length,  $L$ , of  $3 \mu\text{m}$  and a carrier mobility of  $1000 \text{ cm}^2 \text{ V}^{-1} \text{ s}^{-1}$  in the current investigation, the carrier transit time can be approximately calculated as  $t_r = L^2/\mu V_{ds} = 2 \times 10^{-10} \text{ s}$ . Therefore, the photogenerated free carrier lifetime,  $\tau$ , can be assessed as  $1.2 \mu\text{s}$  by combining eqn (6) and (7) at the wavelength of  $1550 \text{ nm}$ . In general, the response time,  $\tau_0$ , is determined mainly by the lifetime of photogenerated free carriers, and can be expressed using the equation  $\tau_0 = (1 + p_t/p)\tau$ , where  $p_t$  and  $p$  are the trapped carrier density and photogenerated free carrier density, respectively.

Therefore, based on the above calculated value of  $\tau$ , the theoretical value of  $\tau_0$  can be estimated to be  $\sim 1.2 \mu\text{s}$ , which is contradictory to our experimentally determined response time ( $\sim 500 \mu\text{s}$ ). This is because the  $\tau$  value is obtained by assuming that the quantum efficiency is  $1$  without any traps of photogenerated carriers. However, the quantum efficiency is known as the fraction of the incident optical power that contributes to the electron-hole pair generation; this value is usually far smaller than  $1$  due to the reflectance of light, insufficient absorption of light resulting from the finite thickness of NWs and anisotropic absorption of light arising from the one-dimensional geometry, *etc*. In addition, there are often many carrier traps for NWs obtained from their large surface-to-volume ratio and unpassivated NW surface. As a result, the response time on the order of hundreds of microseconds here would be in a reasonable range from the estimation above.

## Experimental

### Nanowire growth

InGaAs NWs were synthesized on Si/SiO<sub>2</sub> (50 nm-thick thermally grown oxide) wafer pieces in a two-zone furnace using a chemical vapor deposition method. InAs (99.9999% purity) and GaAs (99.9999% purity) powders were mixed in a designated ratio and loaded into a boron nitride crucible in the upstream of the furnace. The growth substrate, deposited with a 0.5 nm-thick Au film in the thermal evaporator, was positioned in the downstream. H<sub>2</sub> (99.999%) was used as the carrier gas to transport the evaporated source materials to the growth substrate. The temperature in the downstream was first elevated to  $800^\circ\text{C}$  and remained at that temperature for 10 min in order to anneal the Au catalyst. For the single-step growth method, the temperature was then cooled directly to the growth temperature ( $\sim 15$  min after the annealing stopped). Then, the upstream zone was started to be heated. When the source temperature reached the designated value, the growth began. For the two-step growth method, the substrate temperature was first cooled to the nucleation temperature ( $\sim 10$  min after annealing) when the source temperature started to elevate. When the source temperature reached the designated value, the nucleation step began. After 11 min, the downstream was stopped with the heating and started to cool again to a second step growth temperature (approximately 68 min after the heating stopped). During the growth, the flow rate of H<sub>2</sub> was maintained at 100 sccm and the corresponding pressure downstream is  $\sim 1$  torr. The grown nanowires were taken out of the furnace after the system was cooled naturally to room temperature. To synthesize In<sub>x</sub>Ga<sub>1-x</sub>As NWs with different chemical stoichiometries, InAs and GaAs source powders in various mixture ratios (1 : 1, 1 : 3, 1 : 9, and 1 : 14 in wt%) were loaded in a boron nitride crucible. The Au thin films with the nominal thickness of 0.5 nm were used as the catalysts for all the NW growth. Considering the different evaporation velocities of source powders, different source and growth temperatures were used for each mixture ratio. The details are listed in the ESI† Table S1.

## Device fabrication

After CVD growth, the InGaAs NWs were first harvested by sonication in the high-purity anhydrous ethanol solution. Then, the InGaAs NW field-effect-transistors (FETs) were fabricated based on the global back-gated configuration. To be specific, the obtained NW suspension was randomly drop-casted onto the pre-cleaned highly boron doped Si(100) wafer pieces with a resistivity of 0.001 to 0.005  $\Omega$  cm with a 50 nm thick thermally grown gate oxide. The sample was then spin-coated with LOR and AZ5206 photoresist, exposed to ultraviolet light and underwent development. After delineating the source and drain patterns, a 50 nm-thick Ni film was thermally deposited as the contact electrode followed by a lift-off process.

For the NW parallel array devices, the NW arrays were first printed onto the device substrate as reported elsewhere.<sup>44</sup> The processed substrates were then spin-coated with LOR and AZ5206 photoresist through the standard lithography steps, followed by Ni electrode deposition and the lift-off process as mentioned above.

## Material and device characterization

All material characterizations were performed on the NWs obtained in the 0–1 cm region of the growth substrates so that a consistent study could be established. Surface morphologies of the grown NWs were examined using a scanning electron microscope (SEM, FEI/Philips XL30 ESEM-FEG). High-resolution transmission electron microscopy (HRTEM) image of the NWs was observed using a JEOL 2100F transmission electron microscope. The composition of the NWs was determined using an energy dispersive X-ray spectroscopy (EDS) detector attached to the JEOL 2100F. During the EDS measurements, around thirty NWs were randomly chosen as candidates for the EDS point scan in the NW body. All photodetector measurements were performed by using a standard probe station with an Agilent 4155C semiconductor analyzer (Agilent Technologies, Santa Clara, CA, USA) coupled with a 1550 nm laser as the light source whose power was measured by a power meter (PM400, Thorlabs).

## Conclusions

In summary,  $\text{In}_x\text{Ga}_{1-x}\text{As}$  NWs with the controllable stoichiometry and excellent crystallinity have been successively fabricated by a two-step chemical vapor deposition (CVD) method. By configuring them into photodetectors, the photoconducting property of InGaAs NWs towards IR irradiation can be thoroughly studied. It is observed that the two-step CVD grown  $\text{In}_x\text{Ga}_{1-x}\text{As}$  NWs possess much better optoelectronic properties as compared with those of the single-step grown NWs due to the enhanced NW crystal quality and the fewer surface states. On the other hand, when the In concentration increases, the bandgap energy of the NWs can be manipulated for the enhancing photodetector characteristics. Once the  $x$  value is increased to 0.51, the optimal NW photodetection performance towards 1550 nm irradiation occurs. Importantly, high-performance IR photodetectors can be constructed based on

the large-scale NW parallel arrays, which indicates the promising potential of crystalline InGaAs NW arrays for next-generation optoelectronics.

## Conflicts of interest

There are no conflicts to declare.

## Acknowledgements

The authors acknowledge the financial support from the General Research Fund (CityU 11211317) and the Theme-based Research (T42-103/16-N) of the Research Grants Council of Hong Kong SAR, China, the National Natural Science Foundation of China (Grant No. 51672229) and the Science Technology and Innovation Committee of Shenzhen Municipality (Grant JCYJ20170818095520778).

## Notes and references

- 1 J. Wang, M. S. Gudiksen, X. Duan, Y. Cui and C. M. Lieber, Highly polarized photoluminescence and photodetection from single indium phosphide nanowires, *Science*, 2001, **293**(5534), 1455–1457.
- 2 X. Duan, Y. Huang, Y. Cui, J. Wang and C. M. Lieber, Indium phosphide nanowires as building blocks for nano-scale electronic and optoelectronic devices, *Nature*, 2001, **409**(6816), 66–69.
- 3 H. Fang and W. Hu, Photogating in Low Dimensional Photodetectors, *Adv. Sci.*, 2017, **4**(12), 1700323.
- 4 X. Liu, L. Gu, Q. Zhang, J. Wu, Y. Long and Z. Fan, All-printable band-edge modulated ZnO nanowire photodetectors with ultra-high detectivity, *Nat. Commun.*, 2014, **5**, 1–9.
- 5 C. Soci, A. Zhang, B. Xiang, S. A. Dayeh, D. P. R. Aplin and J. Park, *et al.*, ZnO nanowire UV photodetectors with high internal gain, *Nano Lett.*, 2007, **7**(4), 1003–1009.
- 6 D. Zheng, J. Wang, W. Hu, L. Liao, H. Fang and N. Guo, *et al.*, When Nanowires Meet Ultrahigh Ferroelectric Field-High-Performance Full-Depleted Nanowire Photodetectors, *Nano Lett.*, 2016, **16**(4), 2548–2555.
- 7 D. Zheng, H. Fang, P. Wang, W. Luo, F. Gong and J. C. Ho, *et al.*, High-Performance Ferroelectric Polymer Side-Gated CdS Nanowire Ultraviolet Photodetectors, *Adv. Funct. Mater.*, 2016, **26**(42), 7690–7696.
- 8 J. Wallentin, N. Anttu, D. Asoli, M. Huffman, I. Åberg and M. H. Magnusson, *et al.*, InP nanowire array solar cells achieving 13.8% efficiency by exceeding the ray optics limit, *Science*, 2013, **339**(6123), 1057–1060.
- 9 J. A. Del Alamo, Nanometre-scale electronics with III-V compound semiconductors, *Nature*, 2011, **479**(7373), 317–323.
- 10 Z. Yuan, A. Kumar, C. Y. Chen, A. Nainani, B. R. Bennett and J. B. Boos, *et al.*, Antimonide-based heterostructure p-channel MOSFETs with Ni-alloy source/drain, *IEEE Electron Device Lett.*, 2013, **34**(11), 1367–1369.

- 11 L. W. Guo, W. Lu, B. R. Bennett, J. B. Boos and J. A. D. Alamo, Ultralow resistance ohmic contacts for p-channel InGaSb field-effect transistors, *IEEE Electron Device Lett.*, 2015, **36**(6), 546–548.
- 12 A. Nainani, B. R. Bennett, J. Brad Boos, M. G. Ancona and K. C. Saraswat, Enhancing hole mobility in III-V semiconductors, *J. Appl. Phys.*, 2012, **111**(10), 103706.
- 13 Z. Liu, T. Luo, B. Liang, G. Chen, G. Yu and X. Xie, *et al.*, High-detectivity InAs nanowire photodetectors with spectral response from ultraviolet to near-infrared, *Nano Res.*, 2013, **6**(11), 775–783.
- 14 C. H. Kuo, J. M. Wu, S. J. Lin and W. C. Chang, High sensitivity of middle-wavelength infrared photodetectors based on an individual InSb nanowire, *Nanoscale Res. Lett.*, 2013, **8**(1), 1–8.
- 15 L. Ma, W. Hu, Q. Zhang, P. Ren, X. Zhuang and H. Zhou, *et al.*, Room-temperature near-infrared photodetectors based on single heterojunction nanowires, *Nano Lett.*, 2014, **14**(2), 694–698.
- 16 K. Deng and L. Li, CdS nanoscale photodetectors, *Adv. Mater.*, 2014, **26**(17), 2619–2635.
- 17 X. Liu, L. Jiang, X. Zou, X. Xiao, S. Guo and C. Jiang, *et al.*, Scalable integration of indium zinc oxide/photosensitive-nanowire composite thin-film transistors for transparent multicolor photodetectors array, *Adv. Mater.*, 2014, **26**(18), 2919–2924.
- 18 X. Xie and G. Shen, Single-crystalline In<sub>2</sub>S<sub>3</sub> nanowires based flexible visible-light photodetectors with ultra-high photoresponse, *Nanoscale*, 2015, **7**, 5046–5052, DOI: 10.1039/C5TC02043C.
- 19 R. Basori and A. K. Raychaudhuri, Role of Contact and Contact Modification on Photo-response in a Charge Transfer Complex Single Nanowire Device, *Nano-Micro Lett.*, 2014, **6**(1), 63–69.
- 20 J. Miao, W. Hu, N. Guo, Z. Lu, X. Zou and L. Liao, *et al.*, Single InAs nanowire room-temperature near-infrared photodetectors, *ACS Nano*, 2014, **8**(4), 3628–3635.
- 21 F. Li, Y. Meng, R. Dong, S. P. Yip, C. Lan and X. Kang, *et al.*, High-performance transparent ultraviolet photodetectors based on ingazno superlattice nanowire arrays, *ACS Nano*, 2019, **13**(10), 12042–12051.
- 22 D. Li, C. Lan, A. Manikandan, S. P. Yip, Z. Zhou and X. Liang, *et al.*, Ultra-fast photodetectors based on high-mobility indium gallium antimonide nanowires, *Nat. Commun.*, 2019, **10**(1), 1–10.
- 23 P. Ren, W. Hu, Q. Zhang, X. Zhu, X. Zhuang and L. Ma, *et al.*, Band-selective infrared photodetectors with complete-composition-range InAs<sub>x</sub>P<sub>1-x</sub> alloy nanowires, *Adv. Mater.*, 2014, **26**(44), 7444–7449.
- 24 Z. Li, X. Yuan, L. Fu, K. Peng, F. Wang and X. Fu, *et al.*, Room temperature GaAsSb single nanowire infrared photodetectors, *Nanotechnology*, 2015, **26**(44), 445202, DOI: 10.1088/0957-4484/26/44/445202.
- 25 S. Fuchi, Y. Nonogaki, H. Moriya, A. Koizumi, Y. Fujiwara and Y. Takeda, Composition dependence of energy structure and lattice structure in InGaAs/GaP, *Phys. E*, 2004, **21**(1), 36–44.
- 26 M. L. Huang, Y. C. Chang, C. H. Chang, T. D. Lin, J. Kwo and T. B. Wu, *et al.*, Energy-band parameters of atomic-layer-deposition Al<sub>2</sub>O<sub>3</sub>/InGaAs heterostructure, *Appl. Phys. Lett.*, 2006, **89**(1), 53–56.
- 27 A. Jenichen and C. Engler, Stability and band gaps of InGaP, BGaP, and BiInGaP alloys: density-functional supercell calculations, *Phys. Status Solidi B*, 2010, **247**(1), 59–66.
- 28 J. C. Shin, K. H. Kim, K. J. Yu, H. Hu, L. Yin and C. Z. Ning, *et al.*, In<sub>x</sub>Ga<sub>1-x</sub>As nanowires on silicon: one-dimensional heterogeneous epitaxy, bandgap engineering, and photovoltaics, *Nano Lett.*, 2011, **11**(11), 4831–4838.
- 29 Y. Hou, J. R. Liu, M. Buchanan, A. J. Spring Thorpe, P. J. Poole and H. C. Liu, *et al.*, Terahertz generation using implanted InGaAs photomixers and multi-wavelength quantum dot lasers, *Nano-Micro Lett.*, 2012, **4**(1), 10–13.
- 30 H. Tan, C. Fan, L. Ma, X. Zhang, P. Fan and Y. Yang, *et al.*, Single-crystalline InGaAs nanowires for room-temperature high-performance near-infrared photodetectors, *Nano-Micro Lett.*, 2016, **8**(1), 29–35.
- 31 J. J. Hou, N. Han, F. Wang, F. Xiu, S. Yip and A. T. Hui, *et al.*, Synthesis and Characterizations of Ternary InGaAs Nanowires by a Two-Step Growth Method for High-Performance Electronic Devices, *ACS Nano*, 2012, **6**(4), 3624–3630.
- 32 J. J. Hou, F. Wang, N. Han, F. Xiu, S. Yip and M. Fang, *et al.*, Stoichiometric Effect on Electrical, Optical, and Structural Properties of Composition-Tunable In<sub>x</sub>Ga<sub>1-x</sub>As Nanowires, *ACS Nano*, 2012, **6**(10), 9320–9325.
- 33 N. Han, F. Wang, A. T. Hui, J. J. Hou, G. Shan and F. Xiu, *et al.*, Facile synthesis and growth mechanism of Ni-catalyzed GaAs nanowires on non-crystalline substrates, *Nanotechnology*, 2011, **22**(28), 285607.
- 34 H. Kind, H. Yan, B. Messer, M. Law and P. Yang, Nanowire Ultraviolet Photodetectors and Optical Switches, *Adv. Mater.*, 2002, **14**(2), 158–160.
- 35 Z. Zheng, L. Gan, H. Li, Y. Ma, Y. Bando and D. Golberg, *et al.*, A fully transparent and flexible ultraviolet-visible photodetector based on controlled electrospun ZnO-CdO heterojunction nanofiber arrays, *Adv. Funct. Mater.*, 2015, **25**(37), 5885–5894.
- 36 H. Wang, High gain single GaAs nanowire photodetector, *Appl. Phys. Lett.*, 2013, **103**(9), 16–20.
- 37 L. Ma, X. Zhang, H. Li, H. Tan, Y. Yang and Y. Xu, *et al.*, Bandgap-engineered GaAsSb alloy nanowires for near-infrared photodetection at 1.31 μm, *Semicond. Sci. Technol.*, 2015, **30**(10), 105033.
- 38 C. Zhou, X. T. Zhang, K. Zheng, P. P. Chen, W. Lu and J. Zou, Self-Assembly Growth of In-Rich InGaAs Core-Shell Structured Nanowires with Remarkable Near-Infrared Photoreponsivity, *Nano Lett.*, 2017, **17**(12), 7824–7830.
- 39 N. Guo, W. Hu, L. Liao, S. P. Yip, J. C. Ho and J. Miao, *et al.*, Anomalous and highly efficient InAs nanowire phototransistors based on majority carrier transport at room temperature, *Adv. Mater.*, 2014, **26**(48), 8203–8209.
- 40 P. Wang, S. Liu, W. Luo, H. Fang, F. Gong and N. Guo, *et al.*, Arrayed van der Waals Broadband Detectors for Dual-Band Detection, *Adv. Mater.*, 2017, **29**(16), 1–8.

- 41 L. Hu, J. Yan, M. Liao, H. Xiang, X. Gong and L. Zhang, *et al.*, An optimized ultraviolet-a light photodetector with wide-range photoresponse based on zns/zno biaxial nanobelt, *Adv. Mater.*, 2012, **24**(17), 2305–2309.
- 42 S. M. Sze and K. K. Ng, *Physics of Semiconductor Devices*, 3rd edn, Wiley, Hoboken, NJ, 2007.
- 43 N. Han, A. T. Hui, F. Wang, J. J. Hou, F. Xiu and T. Hung, *et al.*, Crystal phase and growth orientation dependence of GaAs nanowires on NixGay seeds via vapor-solid-solid mechanism, *Appl. Phys. Lett.*, 2011, **99**(8), 2011–2014.
- 44 T. Takahashi, K. Takei, E. Adabi, Z. Fan, A. M. Niknejad and A. Javey, Parallel array InAs nanowire transistors for mechanically bendable, ultrahigh frequency electronics, *ACS Nano*, 2010, **4**(10), 5855–5860.
- 45 C. Soci, A. Zhang, X.-Y. Bao, H. Kim, Y. Lo and D. Wang, Nanowire Photodetectors, *J. Nanosci. Nanotechnol.*, 2010, **10**(3), 1430–1449.